

Effects of asphericity and substructure on the determination of cluster mass with weak gravitational lensing

D. Clowe,^{1*} G. De Lucia,² L. King¹

¹*Institut für Astrophysik und Extraterrestrische Forschung der Universität Bonn, Auf dem Hügel 71, 53121 Bonn, Germany*

²*Max-Planck-Institut für Astrophysik, Karl Schwarzschild Str. 1, 85741 Garching, Germany*

Accepted 3000 January 1. Received 3000 January 1

ABSTRACT

Weak gravitational lensing can be used to directly measure the mass along a line-of-sight without any dependence on the dynamical state of the mass, and thus can be used to measure the masses of clusters even if they are not relaxed. One common technique used to measure cluster masses is fitting azimuthally-averaged gravitational shear profiles with a spherical mass model. In this paper we quantify how asphericity and projected substructure in clusters can affect the virial mass and concentration measured with this technique by simulating weak lensing observations on 30 independent lines-of-sights through each of four high-resolution N-body cluster simulations. We find that the variations in the measured virial mass and concentration are of a size similar to the error expected in ideal weak lensing observations and are correlated, but that the virial mass and concentration of the mean shear profile agree well with that measured in three dimensional models of the clusters. The dominant effect causing the variations is the proximity of the line-of-sight to the major axis of the 3-D cluster mass distribution, with projected substructure only causing minor perturbations in the measured concentration. Finally we find that the best-fit “universal” CDM models used to fit the shear profiles over-predict the surface density of the clusters due to the cluster mass density falling off faster than the r^{-3} model assumption.

Key words: Gravitational lensing – Methods: N-body simulations – Galaxies: clusters: general – dark matter

1 INTRODUCTION

Weak gravitational lensing, in which mass in a field is measured by the distortion induced in the shapes of background galaxies, has proven to be a powerful tool in the study of clusters (see reviews by Bartelmann & Schneider 2001; Mellier 1999). With the advent of wide-field, multi-chip CCD cameras, weak lensing shear profiles for clusters have been measured to beyond the virial radius (Clowe & Schneider 2001, 2002; Dahle et al. 2002) with a high signal-to-noise. For many of these clusters, however, there is a disagreement in the cluster mass as measured by weak lensing and by strong lensing, X-ray observations, and cluster galaxy velocity dispersions.

One possible origin for the differences in the mass estimates is the error introduced by fitting spherically symmetric mass models to aspherical structures. Piffaretti et al. (2003) have calculated that imposing a spherical model on a smooth tri-axial cluster can change the ratio of the measured X-ray mass to weak lensing mass by up to 30%. King et al. (2001) investigated the effect of small-scale substructure seen in N-body simulations of clusters and concluded that

the departures from a smooth mass model caused by these substructures do not greatly effect the weak lensing mass measurements.

Another possible origin for the mass estimate differences is the projection of mass structures along the line-of-sight onto the cluster mass in the weak lensing measurements. Foreground and background structures, for which there exists no positional correlation with the cluster, do not produce a bias in the weak lensing measurements (Hoekstra 2003). Filamentary structures extending from the cluster along the line-of-sight can potentially cause an overestimate of the cluster mass from weak lensing, with estimates of the additional mass measured in N-body simulations ranging from a few percent (Cen 1997; Reblinsky & Bartelmann 1999) to over 50% (Metzler et al. 2001). However, these results are obtained by comparing the total mass projected in a cylinder to that contained in a sphere in the N-body simulation, and not by fitting the shear produced by the projected mass with a projected mass model, as is most commonly done for weak lensing mass determinations of clusters.

In this paper we use four high-resolution N-body simulations of massive clusters to study the effects of cluster asphericity, secondary halos, and filamentary structures on the mass profiles measured by weak lensing. In Section 2 we present the simulations and methods used to project the 3-dimensional simulations to 2-

* Currently at Steward Observatory, University of Arizona

dimensional mass maps. We discuss the weak lensing techniques and results in Section 3, and present our conclusions in Section 4. Throughout this paper we assume the cosmology of the simulations ($\Omega_m = 0.3$, $\Omega_\Lambda = 0.7$, $H_0 = 70$ km/s/Mpc, spectral shape $\Gamma = 0.21$, and spectral normalization $\sigma_8 = 0.9$).

2 SIMULATIONS

The simulations used in this work were carried out by Barbara Lanzoni as part of her PhD thesis and is described in Lanzoni et al. (2004) and De Lucia et al. (2004). A suitable target cluster is selected from a previously generated cosmological simulation of a large region. The particles in the final cluster and their closest surroundings are traced back to their Lagrangian region; the original particles are replaced with a larger number of lower mass particles and perturbed using the same fluctuation spectrum of the parent simulation, but now extended to smaller scales (because of the increased dynamical range). Outside this high resolution region, particles with increasing mass are used in order to model the large-scale density and velocity field of the parent simulation. Assuming these new initial conditions, the particle evolution is followed using the code *GADGET*; a full description of the numerical and algorithmic details is given in Springel et al. (2001).

In this work we use four high resolution re-simulations of clusters (named g1, g51, g72, and g8) with masses $\simeq 1\text{--}2 \times 10^{15} M_\odot$. The parent simulation employed is the VLS simulation carried out by the Virgo Consortium (Jenkins et al. 2001; Yoshida et al. 2001). The simulation was performed using a parallel P3M code (Macfarland et al. 1998) and followed 512^3 particles with a particle mass of $7 \times 10^{10} h^{-1} M_\odot$ in a comoving box of size $479 h^{-1} \text{Mpc}$ on a side. We selected an output of the resimulations with total elapsed time equivalent to placing the clusters at $z_{\text{cl}} = 0.2$. This redshift was chosen to match current weak lensing observations of clusters with wide-field cameras. The particle mass in the high resolution region of the final re-simulation is $\simeq 2 \times 10^9 h^{-1} M_\odot$. A standard friends-of-friends algorithm with a linking length $b = 0.2$ was used to find the group of virialized particles. It has been shown that this linking length results in the selection of groups whose overdensity is close to the one predicted by the spherical collapse model (Cole & Lacey 1996).

For each simulation, 30 surface density maps were created by taking 10 independent rotations of the simulations and three orthogonal projections for each rotation and projecting all of the particles in a 13 Mpc cubic box, whose center was the most bound particle of the primary halo. The rotation of the simulations was performed before the selection of particles inside the box. The 13 Mpc box was the maximum size which was fully populated by the high-resolution particles in all of the rotations. The positions of the particles were projected onto a grid of 1300×1300 pixels (each pixel corresponds to 10 kpc) and a triangular shaped cloud (Hockney & Eastwood 1988) weighting function was used to assign the mass to each pixel. The nearest grid point is assigned a weight of $0.75 - dx^2$ and surrounding points are assigned a weight of $0.5 * (1.5 - dx)^2$, where dx is the distance from the sample to the grid point in units of the pixel size.

Shown in Fig. 1 are three orthogonal projections for each cluster, chosen so that the three projections have a large difference in the resulting best-fit surface density profiles. All of the clusters are best described with a triaxial mass model in 3-D, and the direction of the major axis of the mass distribution is fairly constant at all radii with the exception of g72, in which the mass distribution is

best described as a combination of two triaxial systems with major axes closely aligned but offset from one another. The major axes were calculated from the eigenvectors of the matrix $M_{\alpha\beta}$:

$$M_{\alpha\beta} = \sum_i 1^N X_\alpha^i X_\beta^i \quad (1)$$

with $\alpha, \beta = 1, 2, 3$ and X_α^i being the coordinate of the i th particle with respect to the α axis, relative to the center of mass. For simplicity we fixed the center of mass on the most bound particle of each halo and considered all the particles inside the virial radius.

3 WEAK LENSING ANALYSIS

The goal of weak lensing observations is to measure the dimensionless surface mass density of the clusters, κ , where

$$\kappa = \frac{\Sigma}{\Sigma_{\text{crit}}}. \quad (2)$$

Σ is the two-dimensional surface density of the cluster, and Σ_{crit} is a scaling factor:

$$\Sigma_{\text{crit}} = \frac{c^2}{4\pi G} \frac{D_s}{D_l D_{ls}} \quad (3)$$

where D_s is the angular distance to the source (background) galaxy, D_l is the angular distance to the lens (cluster), and D_{ls} is the angular distance from the lens to the source galaxy.

The surface density κ cannot, however, be measured directly from the shapes of the background galaxies. Instead, one can measure the mean distortion of the galaxies by looking for a systematic deviation from a zero average ellipticity. From the distortion one can measure the reduced shear g , which is related to the shear γ by

$$g = \frac{\gamma}{1 - \kappa}. \quad (4)$$

Once the reduced shear is measured from the background galaxy ellipticities, one can then convert the shear measurements to κ measurements, and then to surface mass measurements if one knows the redshifts of the lens and background galaxies, using a variety of techniques (Bartelmann & Schneider 2001; Mellier 1999).

The technique which we are testing with simulations is that of parameterized model fitting, in which the azimuthally-averaged measured shear is fit with radial surface mass profiles from chosen model families. The radial mass profiles are first converted to κ profiles by assuming a mean redshift for the background galaxies, and then to a reduced shear profile using

$$\langle \gamma(r) \rangle = \bar{\kappa}(r) - \langle \kappa(r) \rangle \quad (5)$$

where $\langle \rangle$ indicate the azimuthally averaged quantities and $\bar{\kappa}(r)$ is the mean κ within radius r . From Eqns. 4 and 5, one then has

$$\langle g(r) \rangle = \frac{\bar{\kappa}(r) - \langle \kappa(r) \rangle}{1 - \langle \kappa(r) \rangle}. \quad (6)$$

This is strictly true only for a circular surface mass profile, but should be a good approximation if the change in $\kappa(r)$ along the averaging circle is small compared to 1. The model reduced shear profile is then compared to the measured profile and the parameters of the model varied to obtain the best fit.

The model family we fit to the data is the “universal CDM profile” from Navarro et al. (1997, hereafter NFW). These profiles have a density profile given by

$$\rho(x) = \frac{\delta_c \rho_c}{x(1+x)^2} \quad (7)$$

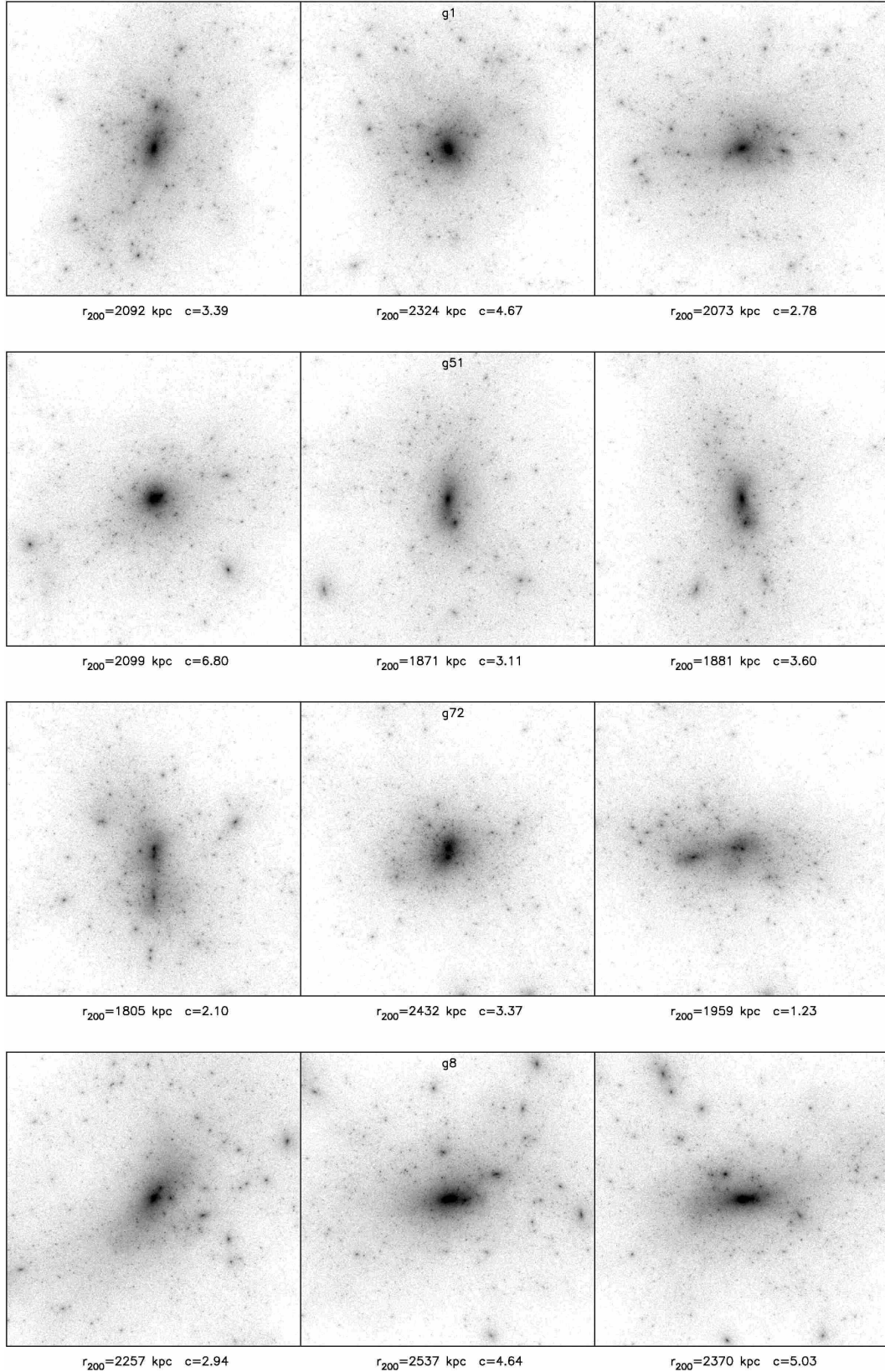


Figure 1. Above are images of the surface mass density for the four simulations. Each simulation is shown with three orthogonal projections, with the left-hand panel projection being rotated about the horizontal axis to obtain the middle panel projection, which is then rotated about the vertical axis to obtain the right-hand panel projection (the horizontal axis of the left-hand image is the vertical axis in the right-hand image). All of the images are shown in a $\sqrt{\log}$ stretch to display structures in both the core and near the image edge.

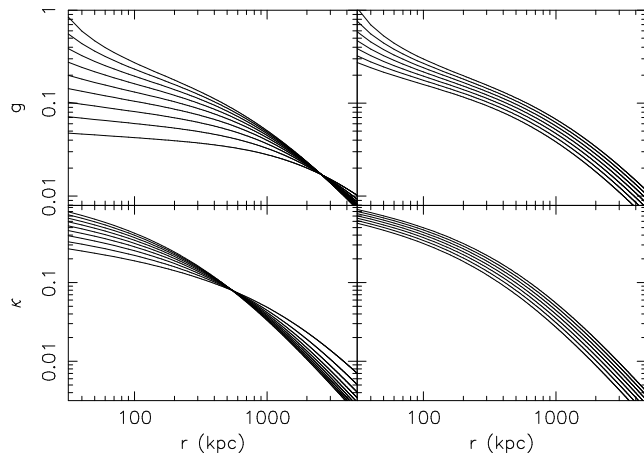


Figure 2. Shown above are the reduced shear, g , and convergence, κ , profiles for NFW models in which one of the two parameters is varied. In the left-hand panels, c varies from 1.0 to 5.0 in increments of 0.5, with r_{200} kept fixed at 2000 kpc. In the right-hand panels, r_{200} varies from 1800 kpc to 2400 kpc in increments of 100 kpc, with c kept fixed at 4.0. As can be seen, increasing r_{200} causes a general increase of both κ and g at all radii, while increasing c causes an increase in both κ and g at small radii, but a decrease at large radii.

where $x = rc/r_{200}$ is a dimensionless radius based on the collapse radius, r_{200} (defined as the radius inside which the mass density is equal to 200 times the critical density, ρ_c) and the concentration, c , and δ_c is a scaling factor which depends on c . Formulas for the surface density, obtained by integrating Eq. 7 along the line of sight, and resulting shear profile can be found in Bartelmann (1996) and Wright & Brainerd (2000), and the reduced shear profile calculated using Eq. 4.

Shown in Fig. 2 are the effects of changing r_{200} and c on the reduced shear profiles and κ profiles of a cluster. Increasing r_{200} results in an increase of both κ and g at all radii. Increasing c , however, results in a shift of mass from the outer parts of the cluster into the core, steepening the rate at which κ decreases with radius. Because the reduced shear measures the change in surface density, increasing the value of c greatly increases the shear of the cluster at all radii inside r_{200} . If two spherical NFW mass structures are superimposed by projection, the measured r_{200} will be relatively insensitive to the alignment of the cores. The measured concentration, however, will depend strongly on how well aligned the cores of the two structures are along the line of sight, with structures which are misaligned by a substantial fraction of the combined r_{200} being detected at extremely low concentration.

3.1 Best-fit NFW profiles

In order to measure the best-fit NFW profiles, the 30 surface density projections for each cluster were converted to κ -maps assuming the clusters are at $z_{cl} = 0.2$ and the background galaxies lie on a sheet at $z_{bg} = 1.0$. The κ -maps were then converted to shear maps by utilizing the fact that both are combinations of second derivatives of the surface potential, and therefore

$$\tilde{\gamma} = \left(\frac{\hat{k}_1^2 - \hat{k}_2^2}{\hat{k}_1^2 + \hat{k}_2^2} \tilde{\kappa}, \frac{2\hat{k}_1\hat{k}_2}{\hat{k}_1^2 + \hat{k}_2^2} \tilde{\kappa} \right) \quad (8)$$

where $\tilde{\gamma}$ and $\tilde{\kappa}$ are the Fourier transforms of the shear and convergence, and \hat{k} are the appropriate wave vectors. The resulting shear maps are then divided by 1 minus the κ -map to produce a reduced

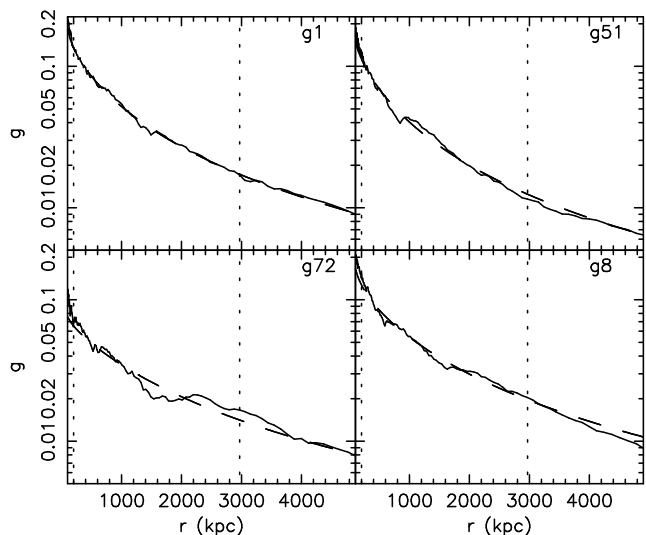


Figure 3. Shown above are the reduced shear profiles for one projection from each of the four simulations. The solid line is the reduced shear from the projection while the dashed line is the best fitting NFW profile. The dotted lines indicate the region over which the fit was performed.

shear map. These can then be discretely sampled and have noise added in order to simulate a background galaxy ellipticity catalog, and then azimuthally averaged to produce a reduced shear profile.

The two primary sources of random noise in weak lensing shear observations are the intrinsic ellipticity distribution of the background galaxies and the superposition of unrelated mass peaks and voids along the line of sight. Neither of these effects give rise to a bias in fitted models (King & Schneider 2001; Hoekstra 2003), and so while the best-fit model for any given noise realization can differ significantly from the best-fit model for the noise-free shear profile, the noise-free model is recovered when averaging over a large number of noise realizations. As a result, we fit the reduced shear profiles for the simulations without adding any noise.

The fits were performed by taking the 2-D shear maps and azimuthally averaging the tangential components of the shear in logarithmically spaced radial annuli about the chosen center. The radial shear profile was then fit with projected NFW shear profiles using χ^2 minimization. While the tangential shear did not have any noise added, we did create a noise estimate for each annulus in order to get a χ^2 statistic from the fitting which could be compared among the different projections and simulations. The noise level was calculated to mimic the average noise from an image which provided 100 galaxies per square arcminute [roughly the usable number density of galaxies in the Hubble Deep Fields (Metcalf et al. 2001)] and 1-D rms shear noise from intrinsic ellipticities of galaxies of 0.2 (0.3 is commonly measured using second moments, Massey et al. (2004) suggest this can be reduced to ~ 0.2 by including higher order moments). These noise estimates are therefore estimates of what is expected from a deep, wide-field image from a space-based telescope of a cluster which has minimal fore- and background structures superimposed.

The shear profiles were created using the location of the most bound particle, which is assumed to be the location of the brightest cluster galaxy. The peak in the projected surface density was typically located within 30 kpc of the most bound particle, and switching the center of the shear profile to the peak position did not greatly effect the parameters of the best fit models. The reduced shear profile was fit over the radial range of $1'$ (197.7 kpc) to

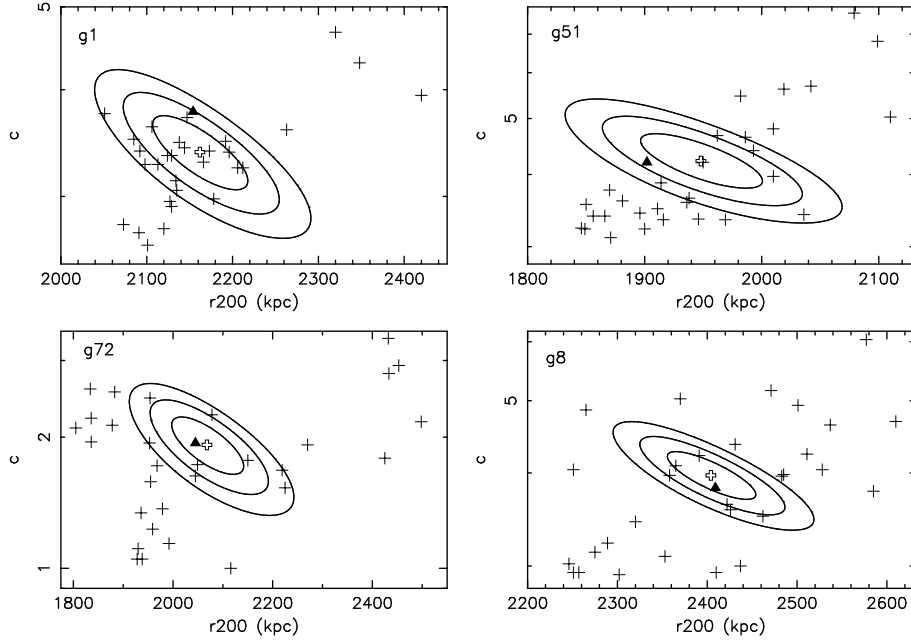


Figure 4. Plotted above, as +, are the best fit values for r_{200} and c for the 30 projections for each simulation. Plotted as the solid triangles are the parameters for the 3-D fit for each simulation, and the open crosses are the fit parameters to the mean of the reduced shear profiles for each simulation. The solid contours are what the 1-, 2-, and 3- σ error contours for a single realization (the open cross) under “ideal” observing conditions with current telescopes.

15' (2.965 Mpc), which is the typical fitting range in recent observations with wide-field cameras (Clowe & Schneider 2002, 2001; Dahle et al. 2002). Inside of 1' the weak lensing signal is typically lost due to crowding from cluster galaxies preventing the measurement of shapes of background galaxies, while the 15' outer radius is determined by the field of view of the mosaic cameras. Hoekstra (2003) suggests that the noise due to projection of unrelated mass structures along the line of sight will increase rapidly at radii larger than 15', and therefore little additional information on the shear profile can be obtained at larger radii.

Shown in Fig. 3 are the reduced shear profiles and best-fit NFW reduced shear profiles for one projection from each of the four clusters. As can be seen, the NFW models provide good fits to the simulations over these regions, and typically are also in good agreement with the reduced shear in the projections at radii outside of the fitting region.

The best-fit NFW model parameters for the projections are shown in Fig. 4, along with the best-fit NFW model to the 3-D density profile and the best-fit NFW model when the shear profiles for the 30 projections are averaged. The parameters for the individual projections span a range of ± 10 -15% in r_{200} and up to a factor of 2 in c , and are, in general, correlated, with higher r_{200} fits also having higher c . The significances of the correlation, as measured by the linear-correlation coefficient, are 99.98%, 99.99996%, 95.12%, and 99.79% for the g1, g51, g72, and g8 simulations respectively.

The value of r_{200} in the projections is also, as expected, strongly correlated with the angular offset between the line-of-sight of the projection and the major-axis of the cluster mass distribution, as can be seen in Fig. 5. The likelihood of the correlation, again measured by the linear-correlation coefficient, arising from noise in uncorrelated data are 7×10^{-9} , 2×10^{-10} , 3×10^{-11} , and 4×10^{-3} for the g1, g51, g72, and g8 simulations respectively. The results for each of the simulations are discussed in detail below.

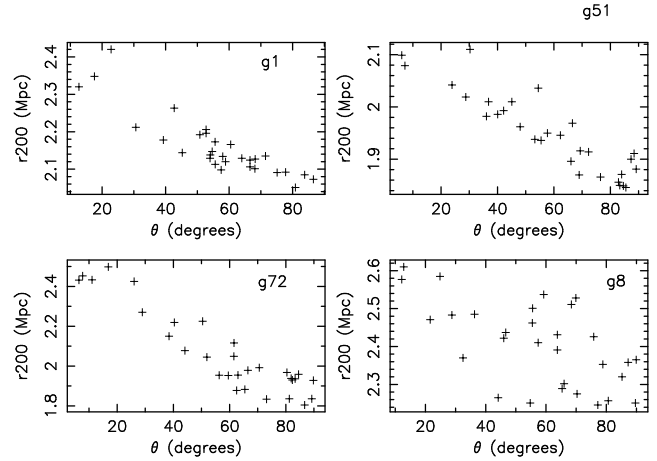


Figure 5. Plotted above are the angular offset between the line-of-sight of the projections and the major-axis of the clusters and the best fit values for r_{200} for the 30 projections for each simulation.

g1 - Most of the projections (27 of the 30) have best-fit models which are clustered in a region between $2050 < r_{200} < 2260$ kpc and $2.5 < c < 3.75$, while the three outlying projections have higher values of both r_{200} and c . The value of r_{200} in the projections is well correlated with the proximity of the line-of-sight through the projection to the major axis in the 3-D mass distribution. Only the three projections with lines-of-sight near the major axis, however, have measured concentrations larger than the 3-D fit, and while the fit to the average of the 30 projections has roughly the same r_{200} as the 3-D fit, its has a markedly lower value of c .

g51 - This cluster has the highest correlation between r_{200} and c in the projection best-fit parameters, which are also strongly correlated with the proximity of the light-of-sight of the projection with the major axis of the 3-D mass distribution. The projection

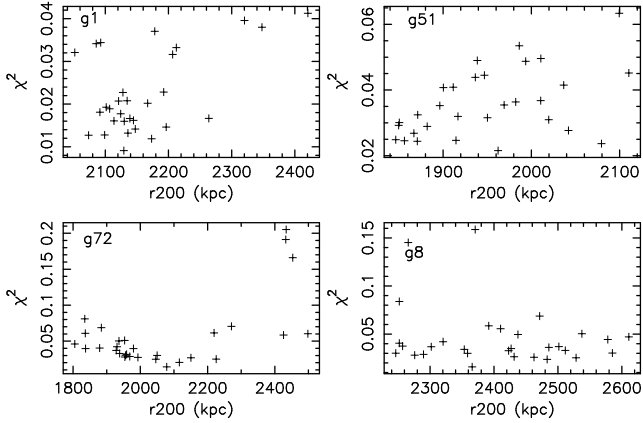


Figure 6. Plotted above are the reduced χ^2 values for the 30 projections for each simulation.

with the highest measured r_{200} has a line-of-sight which is 30° from the major axis, and is due to the projection onto the core of the substructure seen in the lower-left hand corner of the left-hand panel for g51 in Fig. 1 which is normally projected outside of r_{200} and thus not included in the mass. The projections with best-fit r_{200} values near that of the 3-D fit all have lower concentrations than the 3-D fit. The best-fit profile to the average of the projections has a similar concentration as the 3-D fit, but a markedly higher r_{200} .

g72 - The double-core of this cluster results in relatively low concentrations, except when the two cores are projected on top of each other. The high r_{200} projections are those with lines-of-sight near the major axis of the 3-D mass distribution (and the axis connecting the two cores), with the large spread in c being a result of how near the two cores are projected. The mid r_{200} , low c projections are those in which the line-of-sight is near the minor axis of the larger core, while the low r_{200} , (relatively) high c projections have lines-of-sight near the intermediate axis. The r_{200} , c anti-correlation seen in the small r_{200} values is due primarily to the minor and intermediate axes of the larger core being rotated to the minor and intermediate axes of the larger-radii mass distribution. The best-fit profile for the average of the projections is similar in both r_{200} and c to the 3-D profile.

g8 - The large scatter in the best-fit r_{200} and c is a result of the two massive filaments and numerous secondary mass peaks in the outskirts of the simulation region. The larger r_{200} values occur when one of the filaments is projected within r_{200} of the cluster. The higher values of c occur when one of the secondary mass peaks is projected near the cluster core. Due to the crescent-moon shape of the filamentary structure, projections were only able to have one of the two filaments projected onto the cluster, and therefore the number of high r_{200} projections is larger than is found in the other simulations, which have more linear structures, but the fractional increase in surface mass in these projections is smaller compared to the 3-D fit than in the other simulations. This also results in the smallest correlation between r_{200} and the angular offset between the line-of-sight and the major axis. The best-fit profile from the mean shear of the projections is similar in both r_{200} and c to the 3-D profile.

Also shown in Fig. 4 are typical error contours for the NFW model fit from the noise estimates discussed above. As can be seen, the spread in the best-fit parameters among the projections is slightly larger (rms of M_{200} in the projections is $\sim 30\%$ larger than the 1σ errors from the noise estimates, except for g72, for which it's

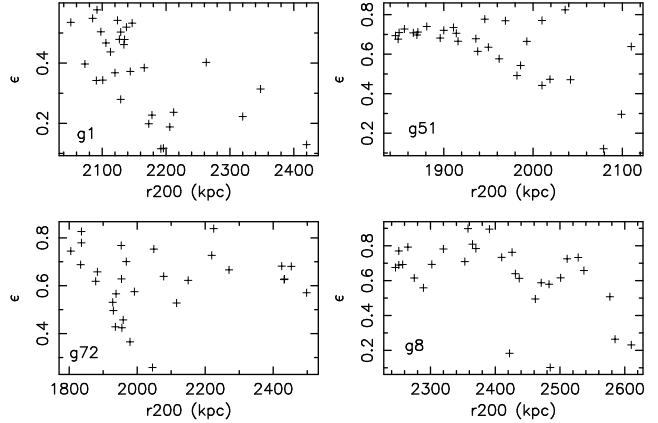


Figure 7. Plotted above are the ellipticities, as defined by Eq. 9 and measured over the region $50\text{kpc} < r < 500\text{kpc}$, for the 30 projections for each simulation. As can be seen, there is in general an anti-correlation between the ellipticity and the measured surface mass, but the mean ellipticity varies among the simulations.

almost twice as large) than the error expected from “ideal” observations which could be taken with current telescopes. The degeneracy between r_{200} and c in the error contours, however, is roughly orthogonal to the correlations from the projections, and so the combined error contours from a single observation would tend to become more circular.

The quality of the fit, as measured by reduced χ^2 between the model and projection's reduced shear profiles, is shown in Fig. 6. While there is a large range in the χ^2 among the projections for a given simulation, and the g72 simulation has a higher χ^2 on average than the rest due to the massive secondary peak, all of the χ^2 s are much smaller than 1. Once noise is added to the shear profile, the reduced χ^2 becomes close to 1 for all of the projections.

3.2 Correlation of mass with ellipticity

One of the effects common to all four simulations is that the higher r_{200} values tend to be measured for projections in which the line-of-sight lies near the major axis of the 3-D mass distribution. Given that the 3-D mass distribution is generally well described by a triaxial model, one might expect that there should exist an anti-correlation between the ellipticity of the central surface mass peak in the projected images and the r_{200} measured by the fit to the shear from that peak. The projections with the highest ellipticity would be those with the major axis in the plane of the sky, and thus have the lowest r_{200} .

We measured the ellipticity of the central mass peak by making a change of variable in the projected NFW equations from $x = rc/r_{200}$ to

$$\xi = x\sqrt{1 - \epsilon \cos(2(\theta - \theta_0))} \quad (9)$$

where ϵ gives the ellipticity and θ_0 is the positional angle. Because this transformation of the surface mass from circularly symmetric to elliptical does not result in an analytic solution for the shear, we measure the ellipticities directly in the surface density maps. Shown in Fig. 7 are the ellipticities for the 30 projections plotted against the r_{200} for the best-fit NFW model. The ellipticities were calculated as the best fit single value of ϵ over the range of 50 to 500 kpc. As can be seen, there is in general an anti-correlation between ellipticity and r_{200} with higher r_{200} generally resulting in lower

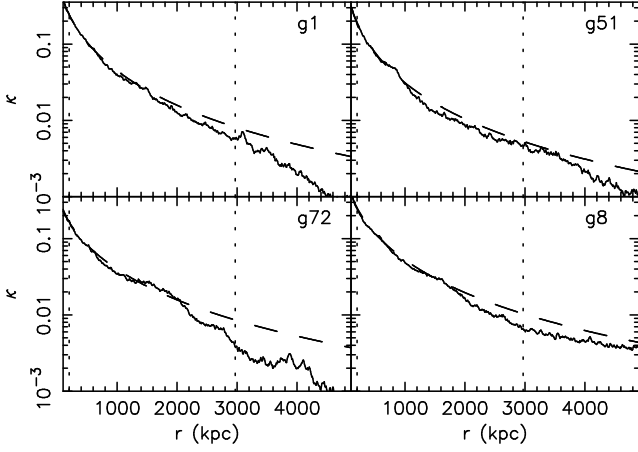


Figure 8. Shown above are the κ profiles for one projection from each of the four simulations, the same projections whose reduced shear profiles are shown in Fig. 3. The solid line is the convergence from the projection while the dashed line is the best fitting NFW profile to the reduced shear. The dotted lines indicate the region over which the fit was performed.

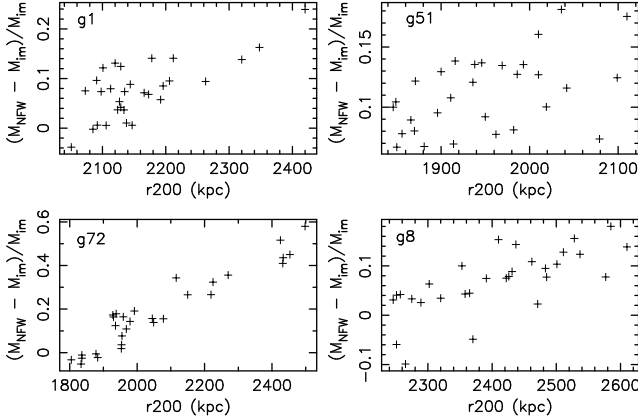


Figure 9. Plotted above are the amounts of excess surface mass within $r \leq r_{200}$ of the best-fit NFW profile to the reduced shear compared with what is actually present in the projection, as a fraction of the surface mass in the projection.

ellipticity. The significance of this correlation, as measured by the linear-correlation coefficient, is 99.6%, 99.3%, 74.3%, and 95.0% for g1, g51, g72, and g8 respectively. The range in the values of ϵ differ for the four clusters, however, and thus there is not a relation which can be used as a generic correction for the observed surface mass.

3.3 Missing surface mass

While the projected NFW profiles provide a good fit to the shear profiles of the clusters, they predict a larger surface density than is observed at large radii. In Fig. 8 are the radial κ profiles for the four simulations whose shears are plotted in Fig. 3, along with the κ profiles for the NFW profiles. As can be seen, the surface density falls off faster at large radius than is predicted by the best-fit NFW profile to the shear. This effect is seen in most of the projections for all four simulations.

In Fig. 9 is plotted the difference in the total surface mass within r_{200} predicted by the best-fit NFW model and that actually

present in the projection. There is a strong correlation between the excess surface mass predicted by the NFW model and the best-fit r_{200} of the model, in that the more massive models have a greater excess surface mass. This is a result of the mass density decreasing faster with increasing radius along the minor and intermediate axes than the major axis of the 3-D mass profile. Because the high r_{200} projections are those with lines-of-sight near the 3-D major axis, the surface density in these projections has the fastest decrease with increasing radius (which is a major cause of the increased χ^2 in the fits, see Fig. 7). As a result, the surface density has the greatest overestimate at large radius, and therefore these projections have a larger overestimate of the total surface mass within r_{200} . For a few projections, this effect is mitigated by the presence of a massive secondary peak or filamentary mass located near the r_{200} outer boundary.

The greatest discrepancy is seen in the cluster g72, which has a large secondary core as the cluster is currently undergoing a major merger event. This secondary core, located 1.65 Mpc from the primary core and therefore within the NFW fit region, results in a low value for the best-fit concentration. While the mass within a sphere with radius r_{200} is independent of the concentration, the total surface mass within a circle of radius r_{200} increases with decreasing concentration. As a result, the low concentration, caused by the presence of the second core, results in a larger over-estimate of the surface density at large radius than is found in the other clusters which have more typical concentration parameters.

The NFW profile has been defined in N-body simulations by only considering the mass density profile within a sphere of radius r_{200} (Navarro et al. 1997). It is therefore not surprising that the mass density profile at larger radii might have a steeper decline than the r^{-3} in the NFW profile. Weak and strong gravitational lensing masses, however, measure the entire mass along the line of sight, including that mass which is not gravitationally bound to the cluster. As such, in order to compare surface densities from lensing to mass estimates from other means, the mass profile outside of r_{200} needs to be included in the models.

These simulations, however, were selected to not have another massive structure within the re-simulated region, and therefore might be biased toward clusters surrounded by an under-dense region. Consequently, the mass profile at large radii might have a steeper profile for these simulations than normal.

4 DISCUSSION

While the best-fit NFW models did, on average, provide a good estimate of the cluster virial mass and mass profile within r_{200} , they overestimated the surface mass density in the projections for radii as small as half the virial radius. This is due to the mass density at large radii falling faster than the $\propto r^{-3}$ predicted by the NFW profile, and while the mass at radii larger than the virial radius are not considered in 3-D models, they constitute a significant fraction of the surface density of the clusters at radii smaller than the virial radius. The greatest discrepancy is seen in the merging cluster system g72, which has unusually low values of the concentration, and therefore a greater overestimate of the mass at large radius.

The cluster for which the best-fit of the mean shear field does not have a similar r_{200} to the 3-D fit is g51, in which the 2-D fit has a $\sim 2\%$ higher value of r_{200} than the 3-D fit. This cluster has a high ellipticity without any significant substructure at large radius and is in virial equilibrium. Under the tests of Jing (2000), this cluster is one in which the NFW profile should provide a measurement

of the total mass of the system. However, as a result of the high ellipticity, combined with the under-density of mass at large radius in these simulations, the mass density decreases with increasing radius much more rapidly along the minor and intermediate axes of the cluster than is assumed by the NFW model. As such, the sphere enclosed by the 3-D r_{200} includes a large volume with densities far below those predicted by the NFW model. Therefore, the r_{200} measured in the 3-D mass distribution underestimates the amount of mass in the cluster, and mean value of the 2-D profiles is a more accurate measurement of the cluster virial mass.

The apparent paradox of the best fit NFW profiles to the shear profiles providing the correct virial masses of the clusters while over-predicting the surface densities, from which the shear profiles are calculated, is a result of the mass sheet degeneracy. As can be seen in Eq. 6, κ profiles related by

$$\kappa'(r) = \kappa(r) + (1 - \kappa(r)) \times \lambda, \quad (10)$$

for any constant λ , produce the same shear profile. This is due to the shear profiles measuring the change in mass with radius, and therefore weak lensing only being able to measure the mass relative to the density at the outer radius of the measured shear region. The imposition of a chosen mass model breaks the mass sheet degeneracy, provided the model has a bijective relation between the shape of the surface density profile and the total mass at a given radius. There is nothing, however, which prevents an incorrect model from being assumed, and therefore measuring a mass profile which differs from the true profile by some value of λ via Eq. 10. In this case, while the NFW model does provide a relation between the surface density slope, which is measured by the shear profile, and the total mass, which is not, at the outer edge of the shear profile, the mass density assumed at large radii is incorrect, and the best fit models over predict the total surface density within the fitting region.

Our result that the mass measured by weak lensing observations is affected mostly by the alignment of the line-of-sight to the major-axis of the cluster, and therefore the small-scale substructure is of minimal importance, is in good agreement with the results of King et al. (2001). This suggests that for the purposes of modeling weak lensing observations, clusters can be adequately described by a smooth, tri-axial mass distribution. Massive sub-halos projected onto the cluster core can, however, perturb the measured concentration parameter for the cluster. The levels of the perturbations of the concentration were typically $\sim 10 - 20\%$, except in the case of the major merger cluster g72, in which case the perturbations were on the order of $50 - 100\%$. Infalling haloes which are outside the virialized region of the cluster can also increase the measured r_{200} , as occurred for one projection of g51, but such projections should be detected in redshift surveys (e.g. Czoske et al. 2002).

Our results that we find, on average, the correct r_{200} , and therefore the correct virial mass, for the clusters is in stark contrast to the results of Cen (1997) and Metzler et al. (2001), who found that weak lensing measurements would be consistently higher than the virial masses of the clusters. The two major differences between our study and theirs are the technique used to measure mass via weak lensing and the size of the projected line-of-sight through the clusters.

Both Cen (1997) and Metzler et al. (2001) simulated weak lensing observations by calculating the aperture densitometry statistic

$$\zeta = \bar{\kappa}(r < r_{\text{ap}}) - \bar{\kappa}(r_{\text{ap}} < r < r_{\text{max}}) \quad (11)$$

which is the mean κ within some radius r_{ap} minus the mean κ in

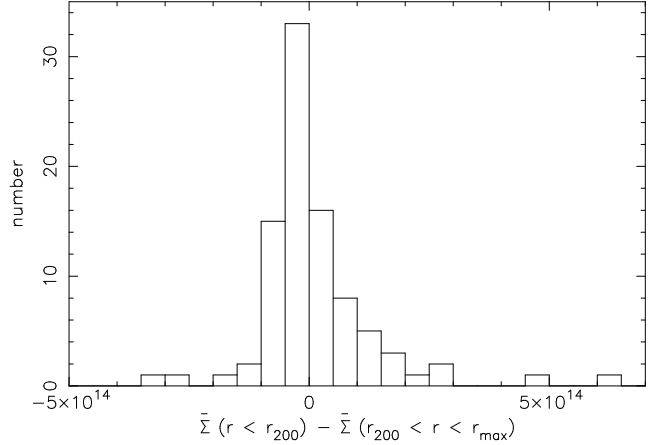


Figure 10. Plotted above are the amounts of excess surface mass within $r < 3\text{Mpc}$ compared to an annular region of $3\text{Mpc} < r < 4\text{Mpc}$ in projections of a 128 Mpc box with the inner 13 Mpc removed.

an annular region from r_{ap} to r_{max} (Fahlman et al. 1994), which can be measured by convolving the shear profile with a specific kernel. Rather than calculating the shear produced by the clusters, both papers estimated ζ directly from the projected images by measuring the $\bar{\kappa}$ within a given radius. However, instead of subtracting off the mean κ within an annular region immediately surrounding the radius used to measure $\bar{\kappa}$, they subtracted off the mean κ measured across all of the simulations. Given that the surface density is still decreasing with increasing radius at $r = r_{200}$, the mean κ in an annular region immediately outside the $r = r_{200}$ aperture is higher than the mean surface density in the rest of the simulated regions. As a result, both papers overestimated ζ for their clusters, and therefore overestimated the cluster mass which would have been measured by this weak lensing technique.

Both papers then compared the ζ values, converted into a surface mass, with cluster models. With this method, the chosen cluster model must have the correct mass profile at all radii, as one must integrate along the line of sight to measure the surface mass density, in order make an accurate comparison. The 5-10% overestimate of the cluster mass from this technique in Cen (1997) is comparable in size, although opposite in sign, to the $\sim 5\%$ difference between surface mass at r_{200} of the the NFW profiles used here and the true surface mass of the simulation. The larger overestimate of cluster mass via weak lensing from Metzler et al. (2001) is a result of their choice of a cluster model, namely a spherical model which has a mean density of $200 \times \rho_{\text{crit}}$ inside a sphere with radius r_{200} , and a zero density outside the sphere. The excess mass which is detected is therefore likely to be that associated with the cluster outside of r_{200} . Indeed, as can be seen in Fig. 9, if Metzler et al. (2001) had integrated an NFW profile to the edge of their simulated regions instead of only out to r_{200} to measure the expected surface mass of the clusters, they would have found that the technique was underestimating, instead of overestimating, the cluster mass.

While we project the cluster in a 13 Mpc box, the projected regions of Cen (1997) (64 Mpc box) and Metzler et al. (2001) (128 Mpc sphere) are much larger. If there is a structure along the line of sight, such as a filament, then the surface mass of the field will increase, and such structures might be more common in the regions around massive clusters. Indeed, this is one of the reasons quoted in Metzler et al. (2001) for why they find a greater over-estimate of the mass via weak lensing than was found in Cen (1997).

In order to test if the 13 Mpc box size causes us to underestimate the mass which would be measured with our weak lensing technique, we selected three clusters from the original simulation the re-simulations were based on. For each cluster, we rotated the particles to obtain 10 independent lines-of-sight, cut out a 128 Mpc box around the cluster, and projected along the three sides to give 30 independent projections per cluster. We then cut out a 13 Mpc box around each cluster, performed the same projections, and subtracted them from the 128 Mpc box projections to obtain the projection of only those structures which would be located outside of the high-resolution region used in the NFW fits. For each projection we then calculated the ζ statistic with $r_{\text{ap}} = 3$ Mpc, the outer radius of our shear fitting region, and $r_{\text{max}} = 4$ Mpc.

These values of ζ , converted into a surface mass by multiplying by $\pi r_{\text{ap}}^2 \Sigma_{\text{crit}}$, are shown as a histogram in Fig. 10. The mean of the ζ distribution is consistent with zero, although with a skew that results in a broader tail to the large positive surface masses. The distribution has a rms of $1.2 \times 10^{14} M_{\odot}$, which is $\sim 5\%$ of the surface mass at this radius for the simulated clusters. The two projections with high values for the increased mass within r_{ap} are both the result of a second, smaller cluster along the line-of-sight.

Thus, expanding the projected region from our original 13 Mpc to 128 Mpc would have only resulted in a small scatter being added to the measured cluster masses, with the exception of the occasional projection which would have a significantly higher mass (up to 25% additional mass, although these simulations were chosen to not have similar mass neighbors so exclude the possibility of two equal mass clusters being projected along the line of sight). These projections with higher projected mass, however, are caused primarily by secondary clusters along the line-of-sight, and should be visible in the form of a concentration of galaxies at redshifts slightly different from the main cluster.

5 SUMMARY

We have fit NFW profiles to 30 surface density projections for each of 4 simulated clusters, and have found that the line-of-sight variations in the projections can lead to dispersions in the parameters of the best-fit models on the order of the errors expected in high-quality weak lensing observations. Most of the dispersion is due to the tri-axial nature of the clusters, and how close the line-of-sight for the projection was to the major-axis of the cluster. For all of the projections, a NFW surface density profile provided a good enough fit so that, with the expected errors in a high-quality weak lensing observation, an observer would measure a reduced χ^2 close to 1.

Further, there is a general correlation between the two parameters in the NFW models, r_{200} and c . This correlation is due largely to the direction of the major-axis of the clusters not varying largely with radius, and thus a line-of-sight near the major axis would have both a large amount of mass projected onto the core of the cluster and an overall increase in the surface density of the cluster at all radii within r_{200} . Additionally, the projection of sub-halos outside the core of the cluster onto the core causes an additional scatter in the best-fit values for the concentration. The level of scatter in the r_{200} and c best-fit models is comparable to the error expected in weak lensing observations using current telescopes in ideal conditions.

There is also an anti-correlation detected between the best-fit r_{200} for a projection and the ellipticity of the cluster in the projection. Because of the variation in ellipticities of individual

clusters, however, no correction for the measured r_{200} based on the measured ellipticity is possible.

The shear fields from the 30 projections for each cluster were averaged, and the best-fit NFW profile was measured. For three of the four clusters, the difference in the value for r_{200} between the 2-D averaged fit and the 3-D fit is within the errors expected due to the finite number of projections. We argue that the difference in the discrepant cluster is a result of the 3-D spherical fit underestimating the virial mass of the cluster due to the high ellipticity of the cluster.

We found that while the NFW profile fitting technique correctly measured the virial mass on average, the predicted surface mass in the images were all overestimated by the best-fit parameters. This is due to the mass density at large radius decreasing faster than the r^{-3} assumed by the NFW model. While the NFW model was defined only out to r_{200} , calculations of the surface mass observed with weak lensing requires integration along the line of the sight of all the mass in the field, even if it has not yet fallen into the cluster. The overestimate of the 3-D density of the NFW profile when integrated beyond r_{200} results in a significant overestimate of the surface density of the clusters at radii as small as one-half of r_{200} . The mass sheet degeneracy, however, allows the model to overestimate the surface density while still providing a good fit to the shear profile.

Finally, we caution that while we expect these results to be true qualitatively for clusters of all masses and redshift ranges, the quantitative results in the figures should be used only as estimates of the magnitude of the effects for clusters of similar mass and redshift as the simulations.

ACKNOWLEDGMENTS

Barbara Lanzoni, Felix Stoehr, Bepi Tormen and Naoki Yoshida are warmly thanked for all the effort put in the re-simulation project and for letting us use their simulations. We also wish to thank Peter Schneider, Felix Stoehr, and Simon White for useful discussions. This work was supported by the Deutsche Forschungsgemeinschaft under the project SCHN 342/3-1 (D. C. and L. K.), the Alexander von Humboldt Foundation, the German Federal Ministry of Education and Research, and the Program for Investment in the Future (ZIP) of the German Government (G. D. L.).

REFERENCES

- Bartelmann M., 1996, A&A, 313, 697
- Bartelmann M., Schneider P., 2001, Physics Reports, 340, 291
- Cen R., 1997, ApJ, 485, 39
- Clowe D., Schneider P., 2001, A&A, 379, 384
- Clowe D., Schneider P., 2002, A&A, 395, 385
- Cole S., Lacey C., 1996, MNRAS, 281, 716
- Czoske O., Moore B., Kneib J.-P., Soucail G., 2002, A&A, 386, 31
- Dahle H., Kaiser N., Irgens R. J., Lilje P. B., Maddox S. J., 2002, ApJs, 139, 313
- De Lucia G., Kauffmann G., Springel V., et al., 2004, astro-ph/0306205
- Fahlman G., Kaiser N., Squires G., Woods D., 1994, ApJ, 437, 56
- Hockney R. W., Eastwood J. W., 1988, Computer simulation using particles. Bristol: Hilger, 1988
- Hoekstra H., 2003, MNRAS, 339, 1155

- Jenkins A., Frenk C. S., White S. D. M., et al., 2001, MNRAS, 321, 372
- Jing Y. P., 2000, ApJ, 535, 30
- King L., Schneider P., Springel V., 2001, A&A, 378, 748
- King L. J., Schneider P., 2001, A&A, 369, 1
- Lanzoni B., Ciotti L., Cappi A., et al., 2004, astro-ph/0307141
- Macfarland T., Couchman H. M. P., Pearce F. R., et al., 1998, New Astronomy, 3, 687
- Massey R., Rhodes J., Refregier A., et al., 2004, ApJ, submitted
- Mellier Y., 1999, ARA&A, 37, 127
- Metcalf N., Shanks T., Campos A., McCracken H. J., Fong R., 2001, MNRAS, 323, 795
- Metzler C. A., White M., Loken C., 2001, ApJ, 547, 560
- Navarro J. F., Frenk C. S., White S. D. M., 1997, ApJ, 490, 493
- Piffaretti R., Jetzer P., Schindler S., 2003, A&A, 398, 41
- Reblinsky K., Bartelmann M., 1999, A&A, 345, 1
- Springel V., Yoshida N., White S. D. M., 2001, New Astronomy, 6, 79
- Wright C. O., Brainerd T. G., 2000, ApJ, 534, 34
- Yoshida N., Sheth R. K., Diaferio A., 2001, MNRAS, 328, 669